Mon. Not. R. astr. Soc. (1986) **219,** 629–655

High-speed photometry of the dwarf nova Z Cha in quiescence

Janet Wood, Keith Horne★† and Graham Berriman★
Institute of Astronomy, Madingley Road, Cambridge CB3 0HA

Richard Wade★ *Steward Observatory, University of Arizona, Tucson, AZ 85721, USA*

Darragh O'Donoghue and Brian Warner *Department of Astronomy, University of Cape Town, 7700 Rondebosch, South Africa*

Accepted 1985 October 22. Received 1985 September 27

Summary. High-speed white light photometry of the cataclysmic variable star Z Cha is used to study the structure of the system and to derive the properties of its components. The white dwarf and bright spot eclipse timings require a mass ratio, $q=M_R/M_{WD}$ of $0.146<q<0.153$ with corresponding inclinations of $81°.9>i>81°.6$. The infalling stream passes through the light centre of the bright spot. If the central luminous object is the white dwarf its mass is $0.54\pm0.01\,M_\odot$ which corresponds to a secondary star mass of $0.081\pm0.003\,M_\odot$. Agreement between colour and brightness temperatures for the white dwarf and bright spot provide a rough confirmation of the 97 pc distance.

We decompose the mean light curve of Z Cha into its disc, bright spot and white dwarf components, and reconstruct the surface brightness distribution of the disc. The brightness temperature distribution shows that the disc is not both optically thick and in a steady state. Arguments are presented which indicate that the disc is optically thin. Under the optically thick assumption, the mass transfer rate through the outer part of the disc exceeds that into the bright spot, of between $10^{-10.23}\,M_\odot$/yr and $10^{-10.63}\,M_\odot$/yr, as indicated by its visual radiation.

The disc radius remains approximately constant but the flux density at orbital hump maximum decreases by ~30 per cent through our observations, which were obtained over a period of 16 day while Z Cha was in quiescence.

1 Introduction

The many spectroscopic and high-speed photometric observations reported of the eclipsing dwarf nova Z Cha attest to its importance in the field of interacting binary stars e.g. Warner 1974; Bailey

★Visiting astronomer: Cerro Tololo Inter-American Observatory, National Optical Astronomy Observatories, operated by Associated Universities for Research in Astronomy, Inc. under contract with the National Science Foundation.

†Present address: Space Telescope Science Institute, Homewood Campus, Baltimore MD21218, USA.

1979; Smak 1979; Ritter 1980; Vogt 1981; Cook & Warner 1984 and Cook 1985. These studies have shown that the accretion disc, the white dwarf at its centre and the bright spot, formed where the gas stream hits the disc, are eclipsed every 107 min by the secondary star, a red dwarf. Such a detailed eclipse structure has allowed the above workers to measure accurately the times of mid-eclipse and the geometry of the system, and to estimate the masses of its components.

The ease with which many light curves can be measured in this short period system also allows the structure and stability of the components to be studied in detail. We present 19 nights of high speed photometry of Z Cha, consisting of 29 white light curves and two simultaneous sets of *UBR* light curves. We use our observations to improve the ephemeris and to get tighter limits on the system parameters. We investigate systematic changes in our data and use the mean light curve to map the intensity of the accretion disc over its surface.

2 High speed photometry

2.1 OBSERVATIONS AND REDUCTION

The observations reported here are summarized in Table 1. They were obtained at Cerro Tololo Inter-American Observatory and the South African Astronomical Observatory between 1984 February 22 and March 10. Z Cha was in quiescence throughout this time. The previous outburst, a normal one, started on January 2 and the next, a superoutburst, started on May 5 (Bateson, private communication, 1984).

The observations at CTIO were made with a three channel photometer consisting of a GaAs photomultiplier tube and two S-20 tubes. The GaAs tube alone was used to obtain 17 white light

Table 1. Journal of observations.

Date	HJD start 2445000+	Cycle	Filter	Telescope
1984 Feb 24	754.55975	73691	W	.91m CTIO
		73692	W	.91m CTIO
1984 Feb 25	755.55460	73704	W	.91m CTIO
		73705	W	.91m CTIO
1984 Feb 27	757.54218	73731	W	.91m CTIO
		73732	W	.91m CTIO
1984 Feb 28	759.35874	73755	W	.75m SAAO
1984 Feb 29	760.40867	73769	W	.75m SAAO
1984 Mar 1	760.53444	73771	W	.91m CTIO
	760.61111	73772	W	.91m CTIO
1984 Mar 2	762.34655	73795	W	.75m SAAO
		73796	W	.75m SAAO
1984 Mar 3	762.53571	73798	W	.91m CTIO
	762.62446	73799	W	.91m CTIO
		73800	W	.91m CTIO
	763.38758	73809	W	.75m SAAO
		73810	W	.75m SAAO
1984 Mar 4	763.56944	73812	W	.91m CTIO
	764.35394	73822	W	.75m SAAO
		73823	W	.75m SAAO
1984 Mar 5	764.56412	73825	W	.91m CTIO
	764.64197	73826	W	.91m CTIO
	765.32885	73835	W	.75m SAAO
1984 Mar 6	765.52304	73838	W	.91m CTIO
		73839	W	.91m CTIO
1984 Mar 7	767.32775	73862	W	1.00m SAAO
		73863	W	1.00m SAAO
1984 Mar 8	767.53068	73865	W	.91m CTIO
		73876	W	1.00m SAAO
1984 Mar 10	769.52707	73892	UBR	1.50m CTIO
		73893	UBR	1.50m CTIO

Table 2.

Filter	λ_{eff} (Å)	RMS Bandwidth (Å)	Extinction (Mags/airmass)	LTT 2511 fν (mJy)
U	3556	213	0.45	12.43
B	4420	373	0.19	11.14
W	4980	1380	0.25	10.07
R	6517	631	0.08	8.17

curves of Z Cha at the 0.91-m telescope during the first 17 nights. All three channels were used on the last two nights to measure Johnson *U* (S-20), Johnson *B* (S-20) and Kron Cousins *R* (GaAs) simultaneously on the 1.5-m telescope. All these observations were obtained with 1 s integration times.

In both the multicolour and white light observations, sky measurements were made approximately every 5 min, and observations of a nearby comparison star 58 arcsec E, 46 arcsec N of Z Cha were used to check the quality of the photometry. These observations and those of several standard stars (Stone & Baldwin 1983) were used to determine the mean extinction coefficients for the run. There were no significant night-to-night variations and the values given in Table 2 were used in the final reduction. No colour correction terms were included. The observations ranged from 1 to 1.5 airmass and were corrected to 1 airmass rather than zero to reduce the effect of any errors in the extinction. (Any comparisons with theoretical flux densities are done after correcting the filter responses to 1 airmass.)

The flux standard LTT 2511 (Stone & Baldwin 1983) was used to calculate the detector sensitivities for each night. A weighted average of its flux over each bandpass (including the effects of one atmosphere) was used as the mean flux for each filter; these are listed in Table 2, along with the characteristics of each filter.

Twelve eclipses were observed at SAAO, nine on the 0.75-m telescope and three on the 1.0-m telescope. An S-11 photomultiplier tube (Amperex 56DVP) was used on both telescopes and all the observations were obtained with 1 s integration times. Sky measurements were made regularly, but no comparison stars were observed. The mean extinction was chosen to be 0.5 mag/airmass and the observations were corrected to zero airmass. We have only used these observations to measure phases of contact and not flux densities. On average the S-11 tube gives 3300 count/s for a star of *V* mag 13.75 on the 0.75-m telescope. To allow easy comparison between the data we used this approximate value to convert the count rates to mJy.

The faint red star 5 arcsec from Z Cha, first noted by Rayne & Whelan (1981), contaminated all the observations, which were made through a 15-arcsec aperture on the 0.91-m telescope and a 13.4-arcsec aperture on the 1.5-telescope. Care was taken to centre the telescope between Z Cha and the red star so that both were always in the field. A spectrum, obtained at the Anglo–Australian Telescope, allowed us to correct all the CTIO data for this contamination. The star, a G or K star, contributed flux densities of 0.003, 0.17, 0.37 and 0.62 mJy in the *U*, *B*, *W* and *R* bands respectively. No correction was made to the SAAO data since we do not use the flux measurements.

Smak (1979) found that the secondary contributed 20–40 per cent of the light at mid-eclipse. He based his calculations on colours measured by Mumford (1971). These colours include a contribution from the red star near Z Cha and therefore caused him to overtake the flux from the secondary star. The secondary star is a late M dwarf contributing most of the infrared light (Bailey *et al.* 1981) and hence only ~1 per cent of the light at 4800 Å (4 per cent of the light in eclipse). We therefore neglected its contribution to the flux density.

2.2 LIGHT CURVES

Fig. 1(a) shows the 17 white light curves observed at CTIO and Fig. 1(b) the *UBR* light curves. The 12 cycles observed at SAAO are plotted in Fig. 1(c). Throughout this paper, phases are calculated using the quadratic ephemeris derived in Section 3.2. The morphology of the multicolour and white light curves is similar to that seen previously (e.g. Warner 1974; Bailey 1979). As the bright spot rotates into view it gives rise to the 'hump' seen between phases −0.38

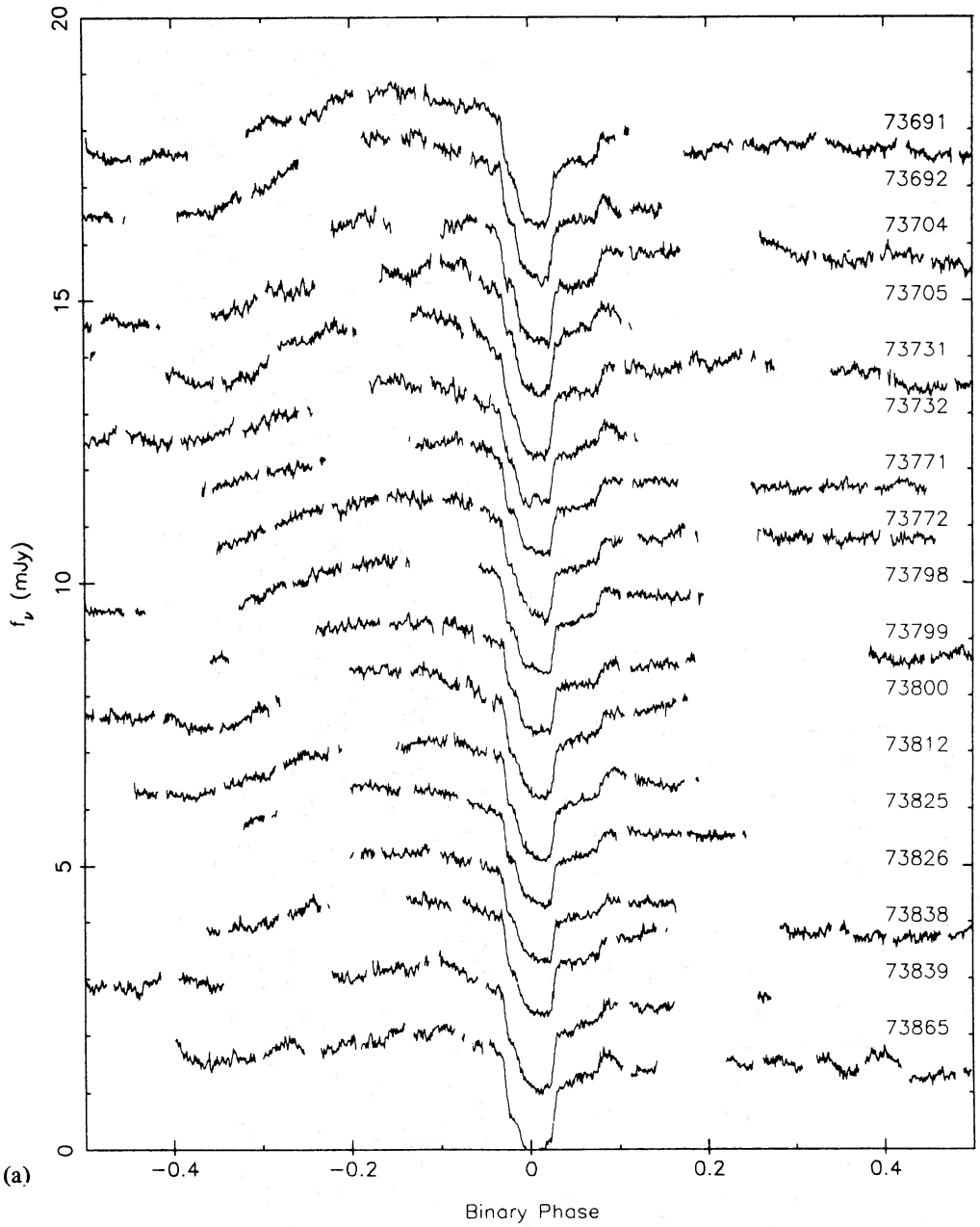

Figure 1. (a) Individual white light curves at 5 s time resolution (observed at CTIO). Each light curve is offset by 1 mJy from the next. The bottom light curve, cycle 73865, is at its measured flux density. (b) *U*, *R* and *B* light curves. *U* and *R* are at 10 s time resolution, *B* is at 15 s time resolution. Each light curve is offset by 3 mJy from the next, with cycle 73893 (B) at its measured flux density. (c) Individual white light curves at 5 s time resolution (observed at SAAO). Each light curve is offset by 1.5 mJy from the next. The bottom light curve, cycle 73876, is at its measured flux density.

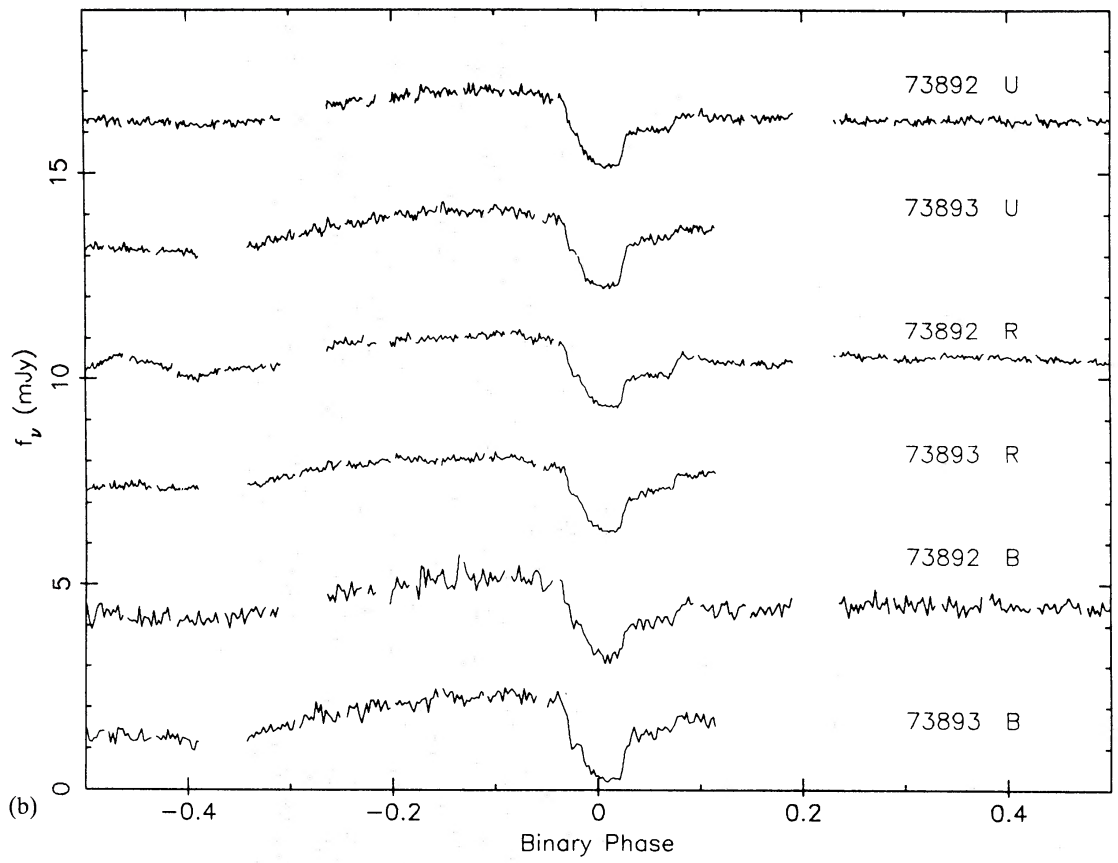

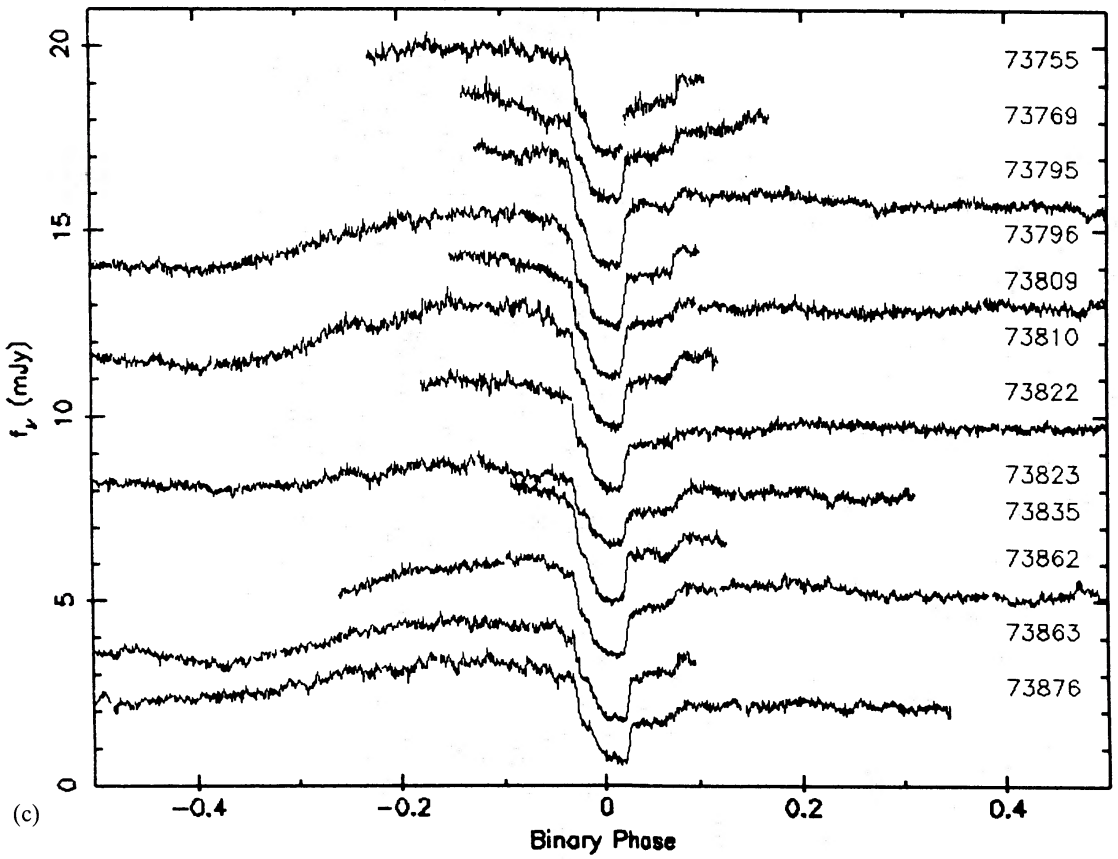

Figure 1 – *continued*

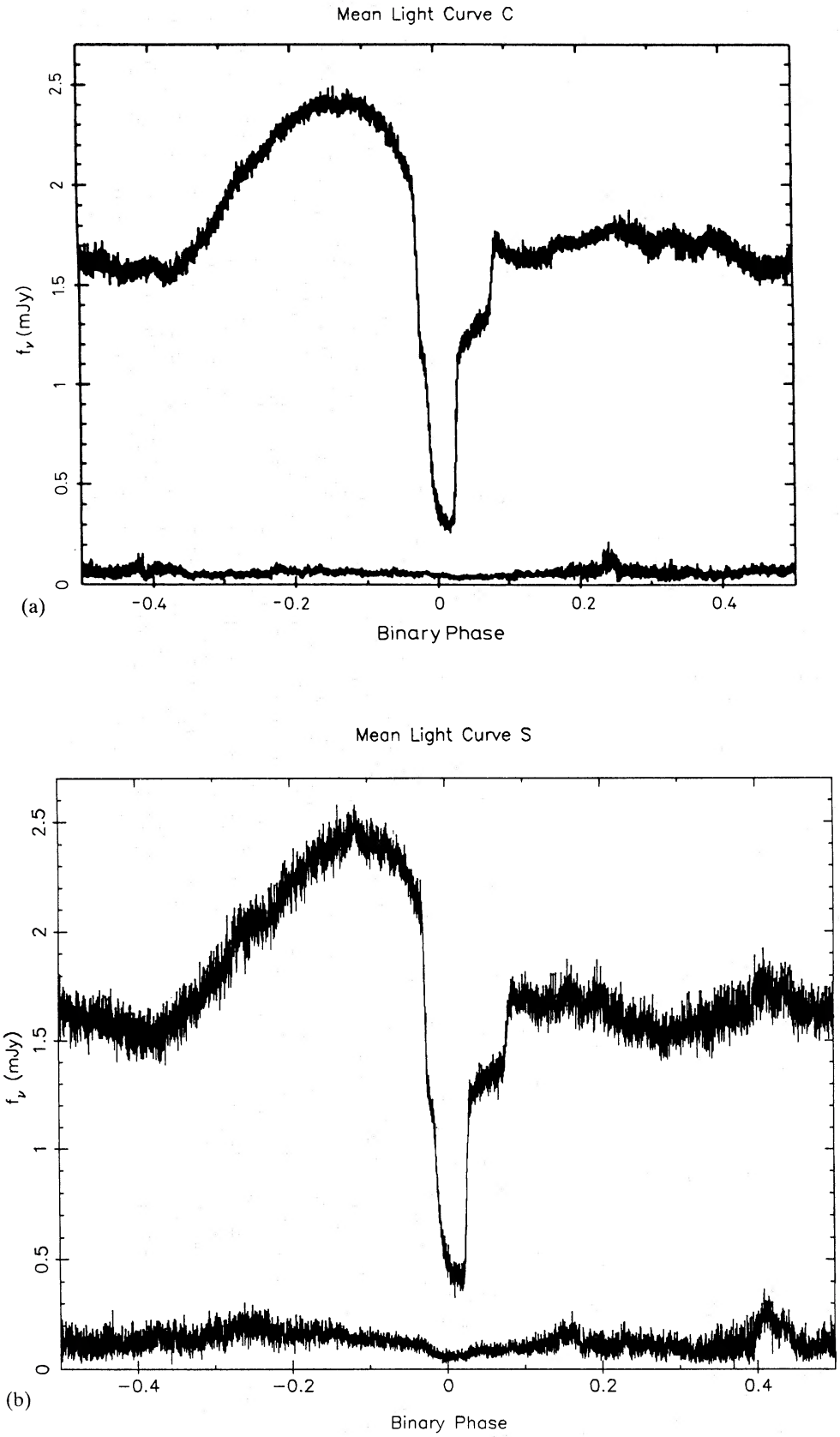

Figure 2. (a) Average of the 17 white light curves observed at CTIO at 1 s time resolution. The lower curve is a measure of the uncertainty in the mean light curve. (b) Average of the 12 white light curves observed at SAAO at 1 s time resolution. The lower curve is a measure of the uncertainty in the mean light curve.

and 0.13. The white dwarf is rapidly eclipsed, in ~55 s, near phase −0.03, followed shortly after by the ingress of the bright spot. Minimum light occurs at phase 0.014. The white dwarf eclipse lasts ~340 s and its egress is followed ~300 s later by the bright spot egress. Each cycle shows the short time-scale flickering characteristic of dwarf novae, and cycle–cycle variability of up to ~0.4 mJy.

The mean light curves were obtained by phase folding the white light curves in Fig. 1(a) and those in Fig. 1(c). The short gaps in the data, which correspond to sky and comparison star measurements, were filled in by linear interpolation since otherwise the cycle–cycle variability of the system would give rise to discontinuities in the mean light curve. The mean light curve of the CTIO data (mean light curve C) is shown in Fig. 2(a) and that of the SAAO data (mean light curve S) in Fig. 2(b). Since the SAAO data were reduced differently from the CTIO data and no standard stars were observed, mean light curve S has been normalized to the flux out of eclipse in mean light curve C. A measure of the uncertainty is also plotted in Figs 2(a) and (b). The flickering is much reduced in the mean light curves and all the features previously described can be seen easily.

3 Geometry of the binary system

3.1 TIMES OF CONTACT

The phases of ingress and egress of the eclipses of the white dwarf and of the bright spot by the secondary star give information about the geometry of the binary system and about the relative sizes of these components.

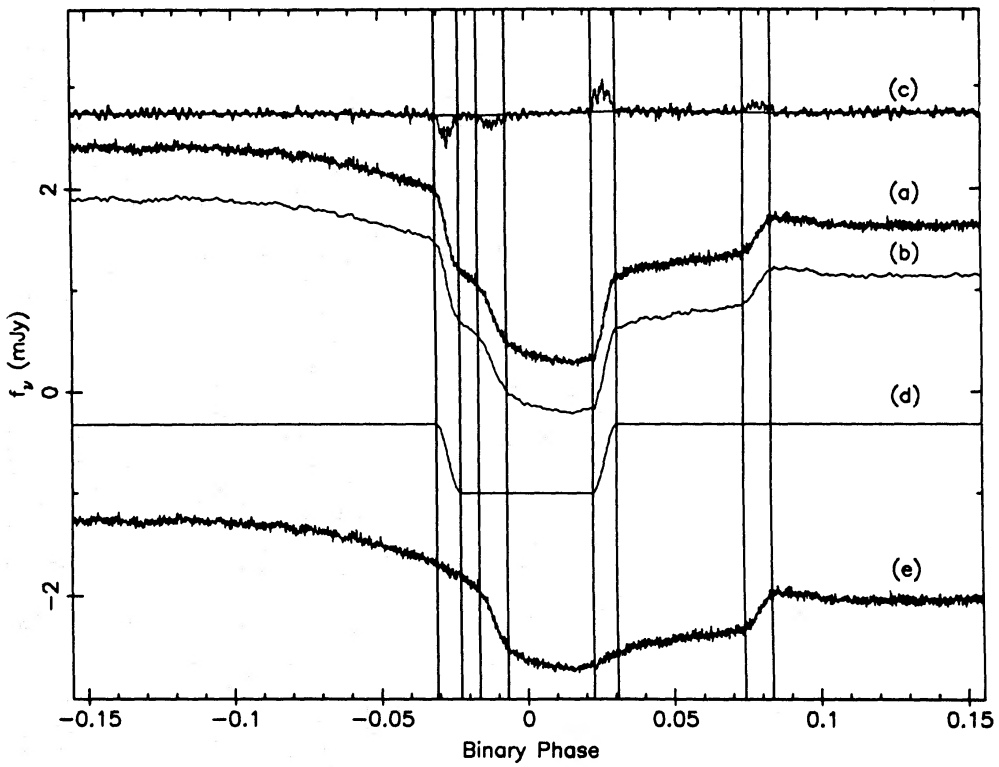

Figure 3. Extraction of the white dwarf eclipse light curve from mean light curve C. (a) Original light curve. (b) Smoothed light curve offset downwards by 0.5 mJy. (c) Derivative of smoothed light curve with spline fit. Both are offset upwards by 2.75 mJy and multiplied by a factor of 10 s. (d) Reconstructed white dwarf eclipse, symmetrized about mid-eclipse and offset downwards by 1 mJy. (e) Original light curve minus white dwarf light curve, offset downwards by 3 mJy. The vertical lines show the contact phases of the white dwarf and the bright spot.

We have measured the eight contact points for each cycle with a technique described in detail by Wood, Irwin & Pringle (1985). Fig. 3 illustrates the steps in the procedure, applied for clarity to mean light curve C, shown in Fig. 3(a). The slope of each light curve increases sharply during the ingress and egress of the bright spot and white dwarf. The contact points of the eclipses of the white dwarf (ϕ_{w1}, ϕ_{w2}, ϕ_{w3}, ϕ_{w4}) and the bright spot (ϕ_{b1}, ϕ_{b2}, ϕ_{b3}, ϕ_{b4}) are found by locating these rapid changes in slope. The original light curve [Fig. 3(a)] is smoothed [Fig. 3(b)] (more smoothing is done for the individual light curves than for the mean) and then differentiated [Fig. 3(c)]. Curve (c) shows the steep slopes during the white dwarf eclipse, and the gentler ones during the bright spot eclipse. The contact points (shown as vertical lines) are placed where the derivative becomes different from a smooth function fitted to the derivative outside white dwarf and bright spot ingress and egress. The fitted function takes account of the fact that the two rapid eclipses are superposed on the gentler eclipse of the disc and on the orbital hump. The measurements of the bright spot correspond to the beginning and end of the eclipse of the compact part only; there is also an extended region which will be discussed in Section 5.1.

The white dwarf eclipse light curve can be reconstructed by assuming that its flux is constant outside ingress and egress and integrating the white dwarf derivative (original derivative minus fitted function) during these times. The symmetrized, reconstructed white dwarf light curve is shown in Fig. 3(d). We will discuss the decomposition of the light curve further in Section 5.1.

The phases of mid ingress and egress ϕ_{wi}, ϕ_{we} were taken to be the phases at which half the light is eclipsed in the unsymmetrized white dwarf eclipse. We define mid-eclipse as the phase $\phi_0=(\phi_{wi}+\phi_{we})/2$. The measured times of mid-eclipse for each cycle are listed in Table 3. The quadratic ephemeris derived in Section 3.2 was used to compute binary phases corresponding to the measured contact times and times of mid-ingress and egress for the white dwarf and bright spot eclipses.

Table 3. Timings of mid-eclipse.

CYCLE	HJED	HJD
73691	2445754.608976	2445754.608349
73692	2445754.683467	2445754.682839
73704	2445755.577539	2445755.576912
73705	2445755.651993	2445755.651365
73731	2445757.588972	2445757.588345
73732	2445757.663416	2445757.662789
73755	2445759.376912	2445759.376285
73769	2445760.419900	2445760.419273
73771	2445760.568916	2445760.568289
73772	2445760.643404	2445760.642777
73795	2445762.356874	2445762.356247
73796	2445762.431416	2445762.430789
73798	2445762.580377	2445762.579751
73799	2445762.654894	2445762.654267
73800	2445762.729399	2445762.728772
73809	2445763.399885	2445763.399258
73810	2445763.474382	2445763.473755
73812	2445763.623359	2445763.622732
73822	2445764.368367	2445764.367740
73823	2445764.442871	2445764.442244
73825	2445764.591842	2445764.591215
73826	2445764.666353	2445764.665726
73835	2445765.336907	2445765.336280
73838	2445765.560351	2445765.559724
73839	2445765.634867	2445765.634241
73862	2445767.348340	2445767.347712
73863	2445767.422828	2445767.422200
73865	2445767.571841	2445767.571214
73876	2445768.391309	2445768.390682

3.2 EPHEMERIS

Cook & Warner (1982) have shown that the eclipse timings of Z Cha obey a non-linear ephemeris. When combined with the published eclipse timings reported by Cook (1983) [based on observations by Warner (1974) and Bailey (1979)] and by Cook & Warner (1984), the present data give an updated ephemeris. Fig. 4 shows the residuals (O–C) calculated with respect to Bailey's (1979) linear ephemeris. These residuals have been calculated on heliocentric ephemeris time since the error in the timings is less than the number of leap seconds on this timebase (the barycentric correction is $\leqslant 1$ s, as Z Cha is close to the ecliptic pole, and has been ignored). A least squares parabolic fit to these data [except those of Cook (1985), which were not then available] shown in Fig. 4 yields the ephemeris (with 1σ errors)

$$HJED = \underset{\pm 6}{2440264.68261} + \underset{\pm 27}{0.0744992335}\,E + \underset{\pm 27}{6.17\times 10^{-13}}\,E^2.$$

An F-test applied to this ephemeris, following the method of Pringle (1975), shows that the quadratic term is significant with 99.9 per cent probability. The period of Z Cha is increasing on a time-scale.

$$P/\dot{P} = 2.46\times 10^7 \text{ yr}.$$

The smoothly increasing period could result, for example, from conservative mass transfer from the secondary star on to the white dwarf (Batten 1973). Using the system parameters derived in Sections 3.3 and 4.2, the required mass transfer rate, $\dot{M} \simeq 10^{-8.4}\,M_\odot/\text{yr}$, is however larger than that observed, even during outburst. The mass transfer rate expected from gravitational radiation is of order $10^{-11}\,M_\odot/\text{yr}$ (Ritter 1980). It seems therefore that conservative mass transfer alone

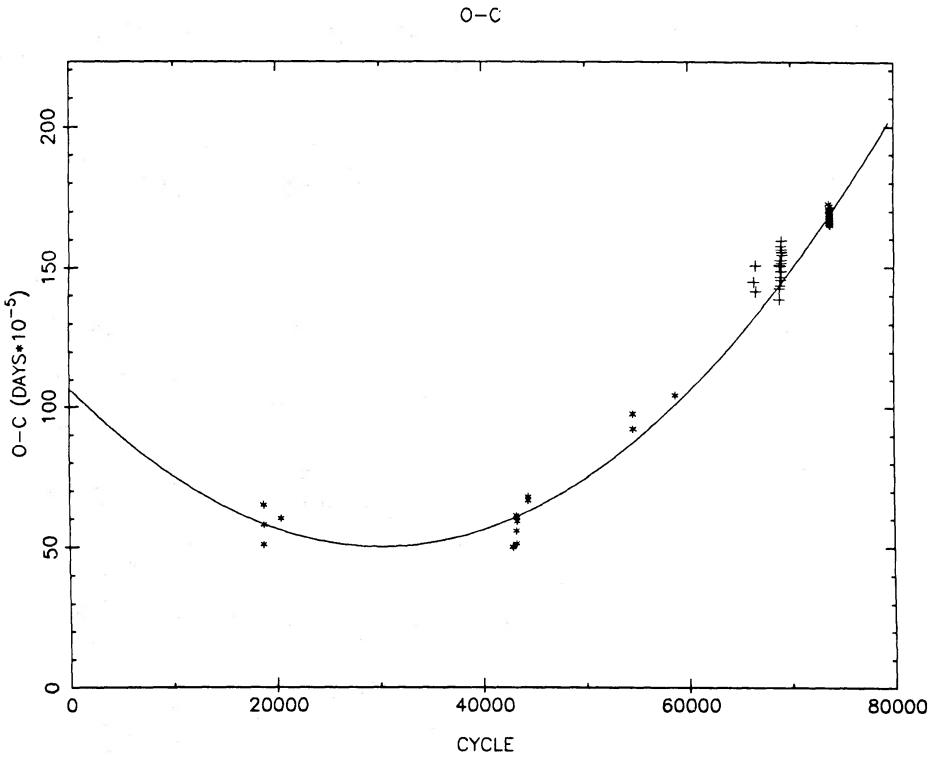

Figure 4. An O–C diagram of the eclipse timings of Z Cha and a parabolic fit to the residuals. Those included in the fit are plotted as ⋆, those not included (from Cook 1985) as +. The residuals are calculated with respect to Bailey's linear ephemeris and a correction to *HJED* is added.

Table 4. White dwarf contact phases.

CYCLE	Φ_{w1}	Φ_{w2}	Φ_{w3}	Φ_{w4}	Φ_{wi}	Φ_{we}
73691	−0.0311	−0.0216	0.0221	0.0308	−0.0263	0.0264
73692	−0.0308	−0.0224	0.0218	0.0311	−0.0266	0.0264
73704	−0.0317	−0.0235	0.0218	0.0374	−0.0276	0.0296
73705	−0.0311	−0.0227	0.0228	0.0325	−0.0269	0.0276
73731	−0.0306	−0.0204	0.0214	0.0309	−0.0255	0.0262
73732	−0.0318	−0.0225	0.0222	0.0306	−0.0272	0.0264
73755	−0.0308	−0.0219	0.0213	0.0300	−0.0264	0.0259
73769	−0.0303	−0.0233	0.0219	0.0306	−0.0270	0.0264
73771	−0.0308	−0.0222	0.0216	0.0312	−0.0265	0.0264
73772	−0.0308	−0.0221	0.0211	0.0309	−0.0264	0.0260
73795	−0.0322	−0.0233	0.0216	0.0301	−0.0273	0.0265
73796	−0.0287	−0.0224	0.0218	0.0314	−0.0262	0.0265
73798	−0.0322	−0.0224	0.0222	0.0311	−0.0273	0.0266
73799	−0.0309	−0.0227	0.0225	0.0308	−0.0268	0.0266
73800	−0.0306	−0.0217	0.0219	0.0305	−0.0262	0.0262
73809	−0.0303	−0.0228	0.0214	0.0314	−0.0269	0.0266
73810	−0.0312	−0.0224	0.0221	0.0300	−0.0268	0.0264
73812	−0.0314	−0.0227	0.0216	0.0308	−0.0270	0.0262
73822	−0.0314	−0.0230	0.0222	0.0306	−0.0272	0.0266
73823	−0.0308	−0.0238	0.0225	0.0308	−0.0272	0.0268
73825	−0.0312	−0.0227	0.0213	0.0305	−0.0269	0.0259
73826	−0.0320	−0.0224	0.0222	0.0306	−0.0272	0.0264
73835	−0.0292	−0.0214	0.0225	0.0303	−0.0259	0.0267
73838	−0.0309	−0.0227	0.0216	0.0308	−0.0268	0.0262
73839	−0.0315	−0.0227	0.0227	0.0312	−0.0271	0.0269
73862	−0.0314	−0.0245	0.0225	0.0312	−0.0274	0.0269
73863	−0.0312	−0.0238	0.0224	0.0301	−0.0273	0.0265
73865	−0.0312	−0.0225	0.0221	0.0309	−0.0270	0.0265
73876	−0.0315	−0.0228	0.0222	0.0303	−0.0273	0.0262
Mean	−0.0310	−0.0226	0.0220	0.0310	−0.0268	0.0266
RMS	0.0007	0.0008	0.0005	0.0013	0.0005	0.0007
Mean Light Curve C	−0.0312	−0.0227	0.0221	0.0308	−0.0270	0.0264
Mean Light Curve S	−0.0308	−0.0227	0.0222	0.0306	−0.0269	0.0267

cannot account for the period change. There may be a third body in the system but many more years of observations will be necessary to determine whether $\dot{P}$ changes sign.

3.3 MASS RATIO AND INCLINATION

Table 4 gives the contact phases ϕ_{w1-4} and mid-ingress (egress) phase ϕ_{wi} (ϕ_{we}) of the white dwarf. The eclipse width $\Delta\phi_w=\phi_{we}-\phi_{wi}$, and ingress (egress) durations Δ_{wi} (Δ_{we}) are given in Table 5. The corresponding phases for the bright spot are given in Tables 6 and 7. The measured phase of mid-eclipse, ϕ_0, is also given for the white dwarf in Table 5.

The derivation of the mass ratio and inclination of Z Cha from observations of the contact phases is by now well known e.g. Fabian *et al.* (1979); Smak (1979) and Cook & Warner (1984). A larger secondary radius R_R/A, where A is the orbital separation, is needed at smaller inclinations to produce a given eclipse width, $\Delta\phi_w$. Because the secondary star fills its Roche lobe, the mass ratio, $q=M_R/M_{WD}$, defines R_R/A and therefore, for a specific white dwarf eclipse width, there is a unique relationship between mass ratio and inclination (Bailey 1979).

Theoretical gas stream trajectories (Lubow & Shu 1975; Fabian *et al.* 1978; Cook & Warner 1984) show that as q becomes larger the streams move closer to the white dwarf, as is shown in Fig. 6(a). At a given mass ratio, each position along the stream has a unique phase of ingress and egress which can be compared directly with ϕ_{bi} and ϕ_{be}. The true mass ratio, and hence inclination, are those for which the infalling stream passes through the bright spot.

Table 5. White dwarf phases.

CYCLE	Δw_i	Δw_e	$\Delta\phi$	ϕ_0
73691	0.0095	0.0087	0.0527	0.00004
73692	0.0084	0.0093	0.0530	−0.00008
73704	0.0082	0.0156	0.0527	0.00101
73705	0.0084	0.0097	0.0545	0.00039
73731	0.0102	0.0095	0.0517	0.00035
73732	0.0093	0.0084	0.0536	−0.00039
73755	0.0089	0.0087	0.0523	−0.00027
73769	0.0070	0.0087	0.0534	−0.00031
73771	0.0086	0.0096	0.0529	−0.00004
73772	0.0087	0.0098	0.0524	−0.00019
73795	0.0089	0.0085	0.0538	−0.00042
73796	0.0064	0.0096	0.0527	0.00015
73798	0.0098	0.0089	0.0539	−0.00031
73799	0.0082	0.0083	0.0534	−0.00008
73800	0.0089	0.0086	0.0534	0.00000
73809	0.0075	0.0099	0.0534	−0.00015
73810	0.0089	0.0079	0.0532	−0.00018
73812	0.0087	0.0092	0.0532	−0.00033
73822	0.0084	0.0084	0.0538	−0.00027
73823	0.0070	0.0082	0.0540	−0.00021
73825	0.0085	0.0092	0.0528	−0.00043
73826	0.0096	0.0084	0.0536	−0.00054
73835	0.0078	0.0078	0.0525	0.00039
73838	0.0082	0.0092	0.0530	−0.00039
73839	0.0088	0.0085	0.0540	−0.00031
73862	0.0068	0.0087	0.0543	−0.00028
73863	0.0075	0.0078	0.0538	−0.00043
73865	0.0087	0.0088	0.0535	−0.00022
73876	0.0087	0.0081	0.0534	−0.00056
Mean	0.0084	0.0090	0.0534	−0.00013
RMS	0.0009	0.0013	0.0009	0.00033
Mean Light Curve C	0.0085	0.0087	0.0534	−0.00027
Mean Light Curve S	0.0081	0.0084	0.0536	−0.00014

The stream trajectories are calculated in the coordinate system rotating with the binary. The X and Y axes are as shown in Figs 5(a) and 6(b). The primary star is at the origin and the secondary star at (1, 0). The equations of motion (Lubow & Shu 1975; Flannery 1975) are solved using a fourth order Runge–Kutta technique and conserving the Jacobi constant to 1 part in 3000.

For each value of q, the phases $\phi_{b1}, \phi_{b2}, \phi_{b3}, \phi_{b4}$ define the region in which the compact part of the bright spot must lie. For each phase, the limb of the secondary star forms an arc (hereafter referred to as a phase arc) when projected along the line-of-sight on to a plane. Fig. 5(a) shows the area in the orbital plane defined by these phase arcs for $q=0.1495$ (for the mean contact phases of the bright spot). A_{kj} are the points defined by the intersection of the phase arcs at ϕ_{bk}, ϕ_{bj}. The light centre LC is the point at the intersection of the phase arcs corresponding to ϕ_{bi} and ϕ_{be}. The overall shape of this region does not depend on the exact value of q. Fig. 5(a) also shows where the stream strikes the edge of the disc, of radius $R_D/A=0.334$ (derived later). Fig. 5(b) shows a similar diagram for the cylinder, of radius $R_D=0.334A$, centred on the white dwarf, perpendicular to the orbital plane; unrolled. On this cylinder Z_{ij} correspond to the phase arc intersections.

The bright spot must come into contact with each phase arc, at least once in some plane. This is automatically satisfied for the case shown [Fig. 5(b)] if the gas stream passes through the light centre and has a finite radius ε of

$0.015<\varepsilon/A<0.025$.

Table 6. Bright spot contact phases.

CYCLE	Φ_{b1}	Φ_{b2}	Φ_{b3}	Φ_{b4}	Φ_{bi}	Φ_{be}
73691	−0.0165	−0.0036	0.0753	0.0830	−0.0100	0.0790
73692	−0.0155	−0.0070	0.0746	0.0823	−0.0113	0.0781
73704	−0.0183	−0.0056	0.0726	0.0845	−0.0127	0.0788
73705	−0.0176	−0.0062	0.0687	0.0803	−0.0120	0.0784
73731	−0.0163	−0.0043	0.0761	0.0861	−0.0100	0.0804
73732	−0.0177	−0.0059	0.0761	0.0836	−0.0108	0.0798
73755	−0.0143	−0.0066	0.0771	0.0839	−0.0102	0.0799
73769	−0.0169	−0.0079	0.0744	0.0822	−0.0125	0.0776
73771	−0.0154	−0.0061	0.0753	0.0827	−0.0111	0.0785
73772	−0.0210	−0.0054	0.0750	0.0834	−0.0120	0.0792
73795	−0.0162	−0.0076	0.0736	0.0845	−0.0124	0.0774
73796	−0.0154	−0.0076	0.0730	0.0823	−0.0119	0.0762
73798	−0.0183	−0.0075	0.0726	0.0831	−0.0119	0.0787
73799	−0.0169	−0.0067	0.0744	0.0836	−0.0116	0.0779
73800	−0.0182	−0.0026	0.0750	0.0833	−0.0100	0.0799
73809	−0.0160	−0.0062	0.0743	0.0820	−0.0117	0.0776
73810	−0.0182	−0.0081	0.0743	0.0848	−0.0136	0.0793
73812	−0.0196	−0.0070	0.0744	0.0853	−0.0120	0.0782
73822	−0.0179	−0.0090	0.0730	0.0806	−0.0134	0.0756
73823	−0.0166	−0.0085	0.0753	0.0861	−0.0127	0.0793
73825	−0.0169	−0.0081	0.0750	0.0830	−0.0128	0.0782
73826	−0.0193	−0.0076	0.0744	0.0836	−0.0130	0.0788
73835	−0.0177	−0.0050	0.0755	0.0845	−0.0128	0.0801
73838	−0.0172	−0.0065	0.0744	0.0825	−0.0125	0.0781
73839	−0.0180	−0.0054	0.0744	0.0836	−0.0120	0.0798
73862	−0.0182	−0.0085	0.0733	0.0834	−0.0136	0.0778
73863	−0.0162	−0.0079	0.0750	0.0830	−0.0131	0.0779
73865	−0.0177	−0.0048	0.0727	0.0813	−0.0117	0.0781
73876	−0.0169	−0.0071	0.0747	0.0881	−0.0116	0.0804
Mean	−0.0173	−0.0066	0.0743	0.0835	−0.0121	0.0785
RMS	0.0014	0.0015	0.0015	0.0016	0.0010	0.0014
Mean Light Curve C	−0.0172	−0.0065	0.0744	0.0831	−0.0114	0.0787
Mean Light Curve S	−0.0169	−0.0067	0.0740	0.0839	−0.0122	0.0781

This stream width is consistent with those expected, as derived from the formula in Cook & Warner (1984).

$$\varepsilon/A = 0.030\,(Te/2800)^{1/2}(M_R/0.081\,M_\odot)^{-1/3}\{(1+q)/1.1495\}^{1/3}.$$

A similar result will hold for each value of q, although the exact numerical values of ε will change.

Assuming that the centre of the stream passes through the light centre of the bright spot, we find $q = 0.1495 \pm 0.0035$. Thus we have

$$0.146 < q < 0.153 \qquad (6.54 < 1/q < 6.85),$$

with corresponding inclinations of

$$81°.9 > i > 81°.6.$$

Several stream trajectories are shown in Fig. 6(a) on an ingress phase versus egress phase diagram. They intersect the observed mid-ingress and egress phases of the bright spot. The uncertainty in the mean mid-ingress and egress phases determines the uncertainties in the mass ratio. Fig. 6(b) shows the stream trajectory for $q = 0.1495$ in the plane of the orbit.

Cook & Warner (1984) found a larger mass ratio range of $5 < 1/q < 7$. They did not take into account the finite width of the stream and allowed the centre of the stream to pass anywhere between LC and A_{13}. We believe that the vertical extent of the bright spot [Fig. 5(b)] when compared with theoretical stream widths means the stream passes almost directly through LC.

Table 7. Bright spot phases.

CYCLE	Δb_i	Δb_e	$\Delta\phi$
73691	0.0129	0.0077	0.0890
73692	0.0085	0.0077	0.0894
73704	0.0127	0.0119	0.0915
73705	0.0114	0.0116	0.0904
73731	0.0120	0.0100	0.0904
73732	0.0118	0.0075	0.0906
73755	0.0082	0.0068	0.0901
73769	0.0090	0.0078	0.0901
73771	0.0093	0.0074	0.0896
73772	0.0156	0.0084	0.0912
73795	0.0085	0.0109	0.0898
73796	0.0078	0.0093	0.0881
73798	0.0108	0.0105	0.0906
73799	0.0102	0.0092	0.0895
73800	0.0156	0.0083	0.0899
73809	0.0098	0.0078	0.0893
73810	0.0101	0.0106	0.0929
73812	0.0126	0.0109	0.0902
73822	0.0089	0.0076	0.0890
73823	0.0081	0.0107	0.0920
73825	0.0088	0.0080	0.0910
73826	0.0117	0.0092	0.0918
73835	0.0127	0.0090	0.0929
73838	0.0107	0.0081	0.0906
73839	0.0126	0.0092	0.0918
73862	0.0096	0.0101	0.0914
73863	0.0082	0.0079	0.0910
73865	0.0129	0.0086	0.0898
73876	0.0098	0.0134	0.0920
Mean	0.0118	0.0090	0.0904
RMS	0.0020	0.0021	0.0012
Mean Light Curve C	0.0107	0.0087	0.0901
Mean Light Curve S	0.0103	0.0099	0.0903

4 The compact components

4.1 THE BRIGHT SPOT

Figs 5 and 6 demonstrate that the light centre of the bright spot moves by less than $\sim\varepsilon/4$ from cycle–cycle. That is, its distance from the white dwarf, R_{BS}, and its azimuth, θ, measured from the line of centres between the two stars, do not change. These quantities are given for each cycle in Table 8. Examination of this table confirms that there are no statistically significant variations in either quantity. The cycle–cycle variations in the measured size of the bright spot can be judged from the dashed lines in Figs 5(a) and (b).

Upper limits on the angular size ($\Delta\theta$), the radial extent (ΔR) and the vertical extent (ΔZ) can also be measured. We define

$$\Delta\theta=(\theta_{23}+\theta_{24}-\theta_{13}-\theta_{14})/2$$

$$\Delta R=(R_{24}+R_{14}-R_{23}-R_{13})/2$$

$$\Delta Z=H_{23},$$

where R_{ij} and θ_{ij} are the radius and azimuth of A_{ij} and H_{ij} the height of Z_{ij} above the orbital plane. The values of $\Delta\theta$, ΔR and ΔZ for each cycle are listed in Table 8. Our values of ΔR and $\Delta\theta$ are small compared to the corresponding measurements made by Cook & Warner (1984), even with their value of q. This could be due to the bright spot being smaller during our observations,

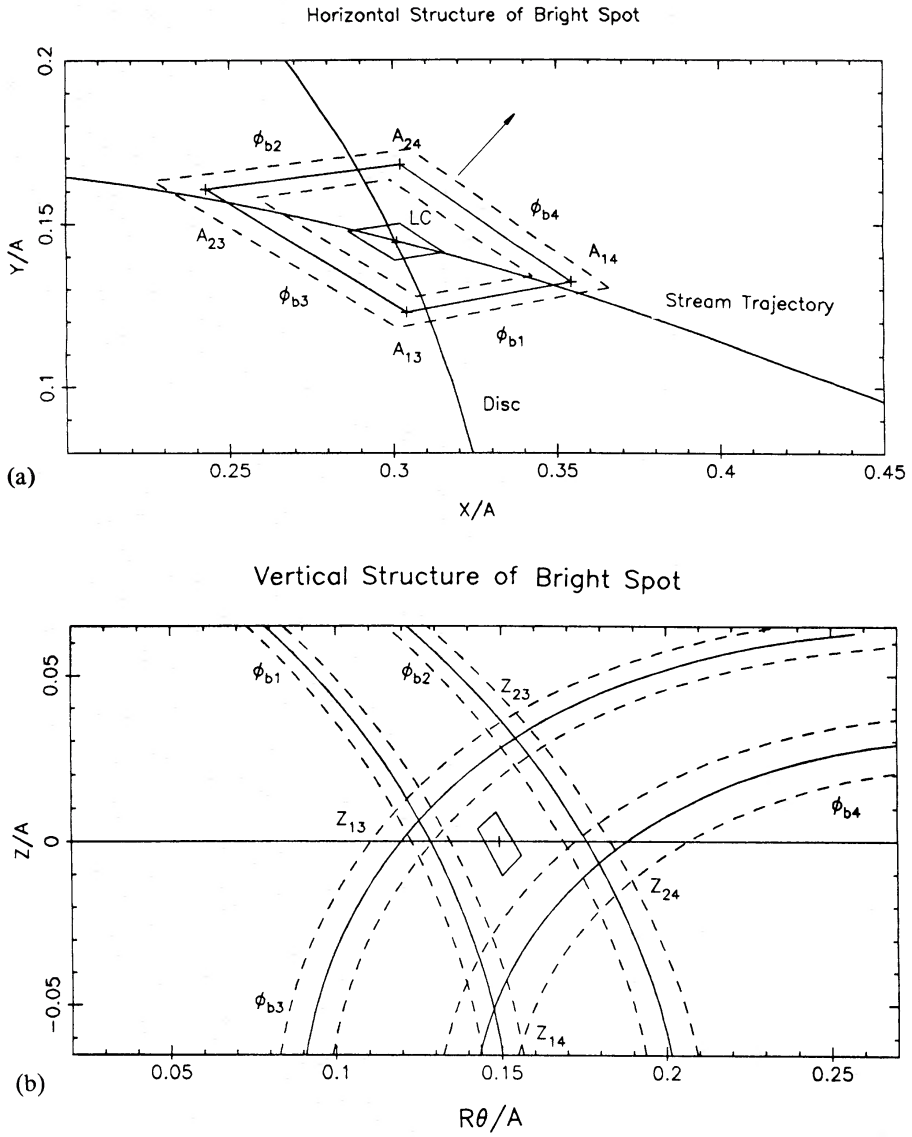

Figure 5. Structure of the bright spot for $q=0.1495$. (a) Region on the orbital plane within which the bright spot lies. The light centre, *LC*, is shown surrounded by a box corresponding to the rms variations in position. The phase arcs corresponding to the bright spot contact phases are shown as solid lines, those corresponding to the rms variations in phases by dotted lines. The intersections of the phase arcs are labelled A_{ij}. The disc of radius $R_D=0.334A$, the stream trajectory and the direction at which the bright spot is at maximum visibility are also shown. (b) Projection of the bright spot phase arcs on to the vertical cylinder of radius $0.334A$. Solid lines correspond to the bright spot contact phases, dotted lines to the rms variations in phase. The light centre is shown surrounded by a box corresponding to the rms variations in its position. The intersections of the phase arcs are labelled Z_{ij}.

or to differences in the measured phases of the various data caused by the different integration times and the different measuring techniques used.

In the mean light curves, the orbital hump begins at phase -0.38 ± 0.008 reaches a maximum at phase -0.13 ± 0.01, shortly before the disc begins to be eclipsed, and finishes at phase 0.13 ± 0.01. This means that, within the uncertainties, the bright spot comes into view for half a cycle and the maximum is mid-way between the start and finish of the orbital hump. The direction at which the bright spot is at maximum visibility is shown in Figs 5(a) and 6(b); it is not along the radial vector through the bright spot. If the emission is produced by an isotropically radiating shock, the shock front must be perpendicular to this direction. A cosine law gives a good fit to the mean orbital

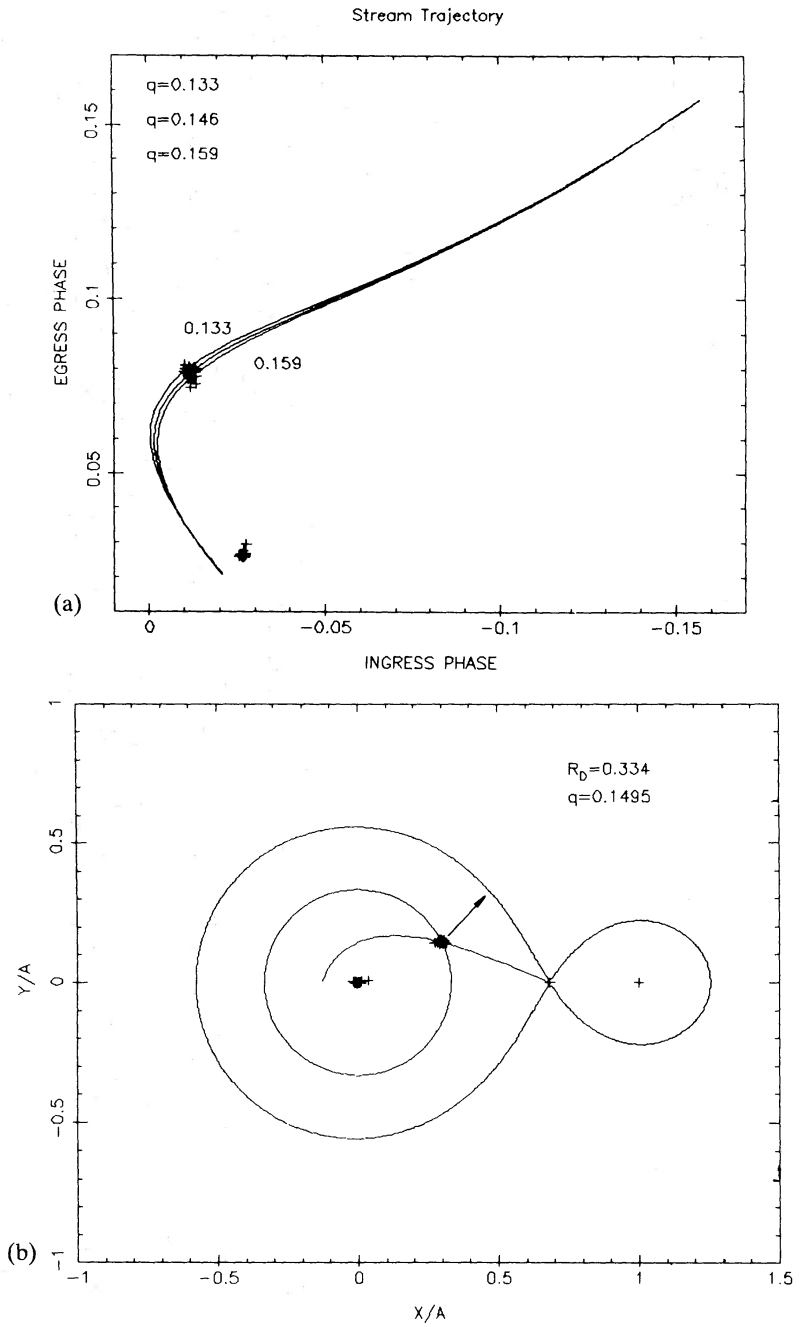

Figure 6. Trajectories of the gas stream from the secondary star. (a) Stream trajectories for $q=0.133$, 0.1495 and 0.159 plotted as a function of ingress phase versus egress phase. The observed phases of mid-ingress/egress of the bright spot and white dwarf are also shown. The streams pass through the bright spot. (b) The system for $q=0.1495$. The observed positions of the light centres of the white dwarf and bright spot are shown with the theoretical gas stream trajectory and a disc of radius $0.334A$. The direction at which the bright spot is at maximum visibility is also shown.

hump. The orbital hump behaves as if it arises entirely from the foreshortening, as the binary rotates, of a bright spot (with no limb-darkening) 'painted' on to the outer rim of the disc.

Assuming that the orbital hump comes from radiation emitted by a circular blackbody of radius ε oriented perpendicular to the orbital plane, we estimate the blackbody brightness temperature, T_{BR}, by equating the observed anisotropic hump flux density $f=0.8\pm0.03$ mJy (see Fig. 8) to the

Table 8. Position and extent of bright spot.

		q=0.1495, Δφ=0.0534			
CYCLE	θ°	R_D/A	Δθ	ΔR/A	ΔZ/A
73691	27.39	0.331	12.8	0.044	0.029
73692	26.43	0.331	8.3	0.045	0.026
73704	25.75	0.334	12.3	0.068	0.037
73705	27.19	0.310	12.6	0.070	0.035
73731	26.46	0.343	11.1	0.056	0.033
73732	25.50	0.341	10.8	0.042	0.028
73755	26.98	0.336	7.7	0.039	0.022
73769	25.53	0.330	8.4	0.045	0.024
73771	26.77	0.332	9.0	0.042	0.026
73772	24.44	0.342	13.9	0.047	0.033
73795	25.72	0.329	8.0	0.062	0.026
73796	26.57	0.320	7.7	0.054	0.023
73798	25.10	0.333	10.3	0.061	0.033
73799	25.75	0.336	9.6	0.052	0.030
73800	27.02	0.332	15.3	0.047	0.033
73809	26.26	0.328	9.6	0.045	0.026
73810	24.09	0.344	9.0	0.059	0.032
73812	24.21	0.346	11.0	0.060	0.035
73822	25.25	0.322	8.4	0.044	0.021
73823	24.89	0.341	7.0	0.060	0.026
73825	25.12	0.338	8.1	0.045	0.026
73826	24.30	0.341	10.4	0.052	0.031
73835	24.55	0.345	11.8	0.051	0.035
73838	25.85	0.333	10.2	0.046	0.028
73839	25.82	0.336	11.9	0.052	0.032
73862	24.49	0.335	8.8	0.057	0.029
73863	24.87	0.334	7.6	0.045	0.024
73865	26.93	0.322	13.2	0.050	0.031
73876	25.55	0.343	8.6	0.074	0.032
Mean	25.68	0.334	10.1	0.052	0.029
RMS	0.96	0.008	2.1	0.009	0.004
Mean Light Curve C	25.75	0.335	10.1	0.050	0.030
Mean Light Curve S	25.67	0.332	9.7	0.057	0.029

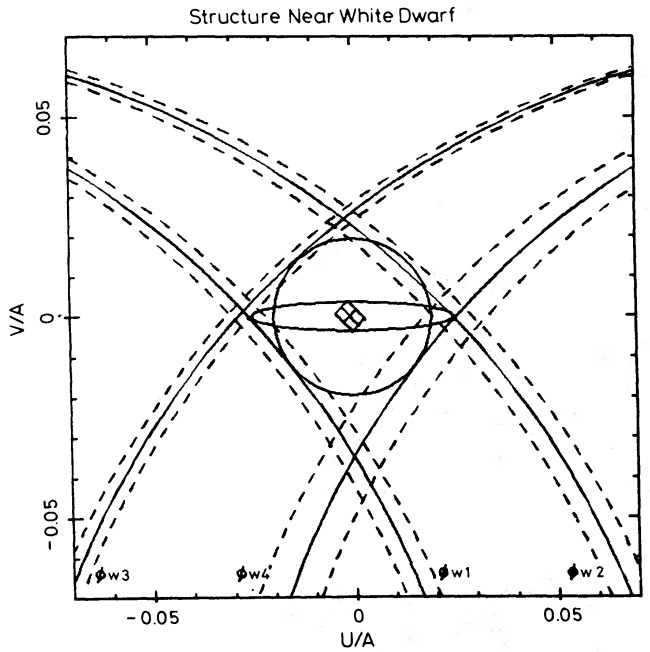

Figure 7. Projection of the white dwarf phase arcs on to the plane perpendicular to the line of sight. U and V are orthogonal coordinates perpendicular to the line-of-sight. U in the plane of the binary. Solid lines correspond to the contact phases of the white dwarf, dotted lines to the rms variations in phase. The projection of the white dwarf and accretion belt are shown for $R_{WD}=0.0195A$ and $R_{ring}=0.025A$. The light centre with its rms error box is also shown.

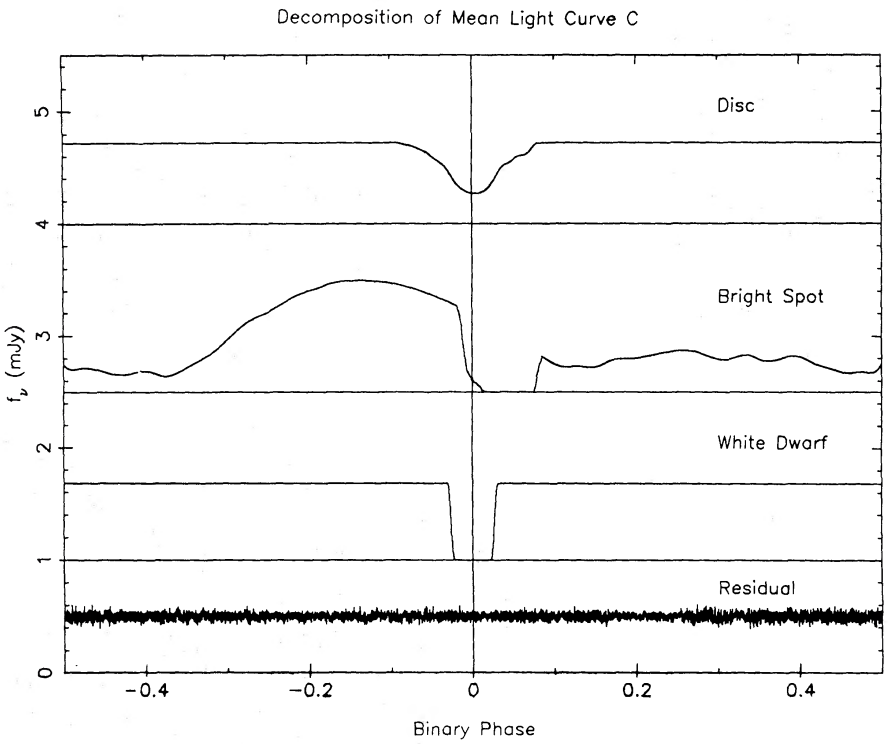

Figure 8. Decomposition of mean light curve C. The separated components of the disc, bright spot and white dwarf are shown. They have been offset but the zero levels are shown for each one. The residual noise is also shown offset upwards by 0.5 mJy.

predicted flux density

$$f=\frac{\int c(\lambda)B_\nu(T_{\rm BR})/\lambda\, d\lambda}{\int c(\lambda)/\lambda\, d\lambda}\times(\pi\varepsilon^2\sin i)/D^2,$$

where $c(\lambda)$ is the response of the bandpass and the $1/\lambda$ weighting gives equal weight to each photon. With a radius $\varepsilon/A=0.020\pm0.005$, ($A=4.2\times10^{10}$ cm, see Section 4.2) and a distance, D, of 97 ± 15 pc (Horne & Cook 1985; Bailey *et al.* 1981) we find $T_{\rm BR}=12\,500\pm650$ K. This is consistent with the colour temperature (calculated using the mean U, B, W and R fluxes of the anisotropic hump) of $11\,300\pm2000$ K. The agreement between these two temperatures provides a rough confirmation of the 97 pc distance.

The structure of this complex component is difficult to determine. It could be radiating from both its sides with most of the light from the side nearest the disc being obscured from our sight, or, it may have an isotropic component radiating from both sides and an anisotropic component radiating from the outer side only. This explains why the flux density in bright spot egress is ~0.3 mJy when the hump would only contribute about 0.15 mJy at this phase. In the first case the bright spot will have a brightness temperature of $13\,100\pm1000$ K, corresponding to a flux density of 1.0 ± 0.03 mJy. In the second case, in addition to the anisotropic component discussed above, the bright spot also has an isotropic component (see Section 5.1 and Fig. 8) of 0.2 ± 0.02 mJy which corresponds to a brightness temperature of 7800 ± 700 K.

The mass transfer rate (corresponding to one component with brightness temperature $T_{\rm BR}$)

into the bright spot, M_{BS}, is given by

$$\dot{M}_{BS}=\frac{\beta\pi\varepsilon^2\sigma T_{BR}^4}{0.5\{V_r^2+(V_\theta-V_{Kep})^2\}}$$

where V_r and V_θ are the components of the velocity of the stream before impact and V_{Kep} the velocity of the edge of the disc. For components of the emission radiating from both sides of the bright spot $\beta=2$, from one side only $\beta=1$. For our parameters, $\dot{M}_{BS}=10^{-10.28\pm0.05}\,M_\odot$/yr for the first case and $\dot{M}_{BS}=10^{-10.54\pm0.09}\,M_\odot$/yr for the second case. Since the model in which the bright spot radiates isotropically has to produce more light (part of which is obscured) this model corresponds to the highest $\dot{M}_{BS}$.

4.2 THE CENTRAL OBJECT

The central object, previously called the white dwarf, could actually be made up of a white dwarf, possibly surrounded by a spherical boundary layer, and in addition a luminous ring of material around its equator. Such thin, flat boundary layers have been discussed in many papers e.g. Lynden-Bell & Pringle (1974) and Pringle (1977). The phases of ingress and egress of the eclipse of the central object do not distinguish between these alternatives, but do give limits to the radius of each component, in just the same way as done for the bright spot. Fig. 7 shows, as solid lines, the phase arcs corresponding to ϕ_{w1}, ϕ_{w2}, ϕ_{w3}, ϕ_{w4} in a plane perpendicular to the line-of-sight (i.e. in the plane of the sky) for $q=0.1495$. In this plane the projection of the central sphere and the ring are the same at all phases. The maximum radius, R_{ring}, of the ring is clearly always larger than that of the central sphere, R_{sph}. As can be seen from Fig. 7, the maximum possible radius of the central sphere (for $q=0.1495$) is $R_{sph}/A=0.0195\pm0.0004$, with a ring of radius $R_{ring}/A\leqslant0.025\pm0.0003$. The uncertainties given are calculated using a Monte Carlo routine propagating the uncertainties in phase, σ (where $\sigma=\text{rms}/\sqrt{N}$, and N is the number of observations). Given the uncertainties the sphere or the ring alone could satisfy all the ingress/egress conditions.

Fig. 7 shows that the observed radius of the central object varies from cycle–cycle by ~10 per cent, which is approximately that expected from statistical fluctuations due to photon noise and flickering. It is therefore likely that the central object is the white dwarf, as also found for HT Cas by Patterson (1981), and we will henceforth treat it as such. We do not apply any corrections for limb darkening to our measured ingress/egress phases (and hence the measured radii) of the white dwarf, since our measuring method will not significantly underestimate the length of ingress/egress (*cf.* Patterson 1981). The position of the light centre of the central object indicates that the lower hemisphere of the white dwarf is not occulted by the disc and hence the inner region of the disc ($R\leqslant R_{WD}/\cos i\sim7\,R_{WD}$) is optically thin.

For $R_{WD}/A=0.0195\pm0.0004$ and our usual parameters we find, for a blackbody, $T_{BR}=11\,800\pm500$ K. Using the mean U, B, W and R fluxes of the white dwarf to get a colour temperature which reproduces these fluxes in each bandpass, we find, the blackbody colour temperature $T_{col}=10\,900\pm1800$ K. If the white dwarf is non-luminous except around its equator its radius could be as large as R_{ring}. The maximum brightness temperature, T_{max}, of the white dwarf (within 2σ limits of the colour temperature) is ~15 500 K. Thus the fraction, F, of the white dwarf surface ($R_{WD}=R_{sph}$) which is luminous is given by

$$F\geqslant B_\nu(T_{col})/B_\nu(T_{max})\simeq0.3.$$

Since $(R_{ring}/R_{sph})^2$ is small, only 1.6, this means a large fraction of the white dwarf's surface must be luminous and would therefore lie outside the limiting phase arcs for $R_{wd}>R_{sph}$; hence $R_{WD}=R_{sph}$. Ours is a somewhat more stringent limit on R_{WD} than that found by Cook & Warner (1984), who assumed that the white dwarf could be as large as the ring.

Table 9. Binary parameters.

q	0.1495 ± 0.0035
i	81.7 ± 0.13
$M_{WD}/M_\odot$	0.544 ± 0.012
$M_R/M_\odot$	0.081 ± 0.003
$R_{WD}/R_\odot$	0.0124 ± 0.0003
$R_R/R_\odot$	0.149 ± 0.002
$A/R_\odot$	0.634 ± 0.005
K_W (km/s)	55.5 ± 1.4
K_R (km/s)	371.0 ± 2.7
R_{L1}/A	0.684 ± 0.002
R_D/A	0.334 ± 0.008
$\dot{M}_{RS}$ ($M_\odot$/yr)	$10^{-10.43\pm0.2}$

Given the white dwarf radius R_{WD}/A and the mass ratio q, Kepler's third law requires that A^3 is proportional to M_{WD}, and hence that R_{WD} is proportional to $M_{WD}^{1/3}$. The intersection of this relation between M_{WD} and R_{WD} with the Hamada–Salpeter (1961) mass–radius relation for cold white dwarfs gives A and M_{WD} simultaneously. The two relations intersect at a steep angle, so that A and M_{WD} are well constrained. For $R_{WD}/A=0.0195\pm0.0004$, and $q=0.1495$ we find $M_{WD}=0.54\pm0.01\,M_\odot$. Table 9 shows the corresponding values of A, R_R, i, the semi-amplitudes of the radial velocities of the white dwarf and the secondary star (the K velocities K_W, K_R) and M_R; the errors given are propagated from the uncertainties (σ) in the mean phases with a Monte Carlo routine. An interesting consequence of this white dwarf mass is that it allows the secondary star to have a mass of $M_R=0.081\pm0.003\,M_\odot$ which is close to the lower mass limit of the hydrogen burning main sequence. If, however, the measured radius of the central object does include a boundary layer, we will have underestimated the masses. A 10 per cent change in the radius would cause approximately a 10 per cent change in the masses.

Our values of M_{WD} and M_R differ greatly from those based on the K velocities measured from emission lines in spectroscopic data (e.g. Ritter 1980; Vogt 1981). The observed K velocity does not actually correspond to K_W since the radial velocity measured from the emission lines does not have the correct phase with respect to the eclipse (Marsh & Horne, in preparation 1986). The observed values of $K_W\sim87\,\mathrm{km\,s^{-1}}$ are much larger than those predicted by our model.

5 The quiescent disc

5.1 DECOMPOSITION OF THE MEAN LIGHT CURVE

So far, we have considered only the properties of the bright spot and the white dwarf, not of the accretion disc itself. A decomposition of mean light curve C [Fig. 2(a)] into the individual components brings to light the shape of the eclipse of the disc.

The white dwarf is easily removed from the mean light curve using the technique described in Section 3.1. The reasonable assumption that its eclipse is symmetric gives a mean white dwarf flux density of 0.66 mJy. The resulting eclipse of the bright spot and disc is shown in Fig. 3(e). The bright spot can be subtracted in a similar fashion but care must be taken to account properly for the orbital hump. The light curve in Fig. 3(e) consists not only of the eclipse of the disc and bright spot, but also of the foreshortening of the bright spot as it rotates away from the line of view after phase ~-0.13. What follows describes how the effects of this foreshortening are taken into account. The procedures described treats the flux density of the disc, f_{disc}, and the bright spot contact phases, ϕ_{bj}, as free parameters, and tests whether the resulting disc light curve is continuous.

If the disc is circular with the bright spot at its edge, the eclipse must occur between phases

± 0.089, for $q=0.1495$ and $R_D/A=0.334$. Particles in a disc of this radius move essentially in the gravitational field of the white dwarf alone, and so they do move in approximately circular orbits (Paczynski 1977). A spline fit to the uneclipsed data bridges the eclipse and describes the light curve of the foreshortened bright spot plus the constant contribution of the disc, f_{disc}.

Subtraction of a trial value of f_{disc} from the spline fit gives the light curve of the uneclipsed bright spot. This component is subtracted from the light curve in Fig. 3(e), but only outside the eclipse of the bright spot. The light remaining is that of the disc alone, except during the ingress and egress of the bright spot. Now the ingress and egress can themselves be constructed by the same procedure used to reconstruct the white dwarf (Section 3.1), and subsequently subtracted from this light curve. The reconstructed ingress and egress of the bright spot automatically contain the contribution from the change in the orbital hump during these times.

The disc light curve produced by this procedure may however exhibit discontinuities at ϕ_{b1} and ϕ_{b4}, because the fluxes of the uneclipsed bright spot and the ingress and egress fluxes of the bright spot are determined independently, but both are subtracted from Fig. 3(e) (in different phase regions of course). Such discontinuities do not automatically imply that the trial flux density of the disc is incorrect as the bright spot may contain an extended component, in addition to the compact one measured previously. This extended component may be, for example, a tail extending around the rim of the disc, or a halo surrounding a core, but whatever its origin it makes the durations of ingress and egress somewhat longer. The procedure was carried through with the contact phases as free parameters for each f_{disc}. Physically plausible parameters, those which allow the light curve of the disc to be continuous, are found empirically to lie in a small range, as follows:

$0.70\,\text{mJy} < f_{disc} < 0.72\,\text{mJy}$

$0.0146 < \phi_{b2} < 0.0165$

$0.0698 < \phi_{b3} < 0.0752$

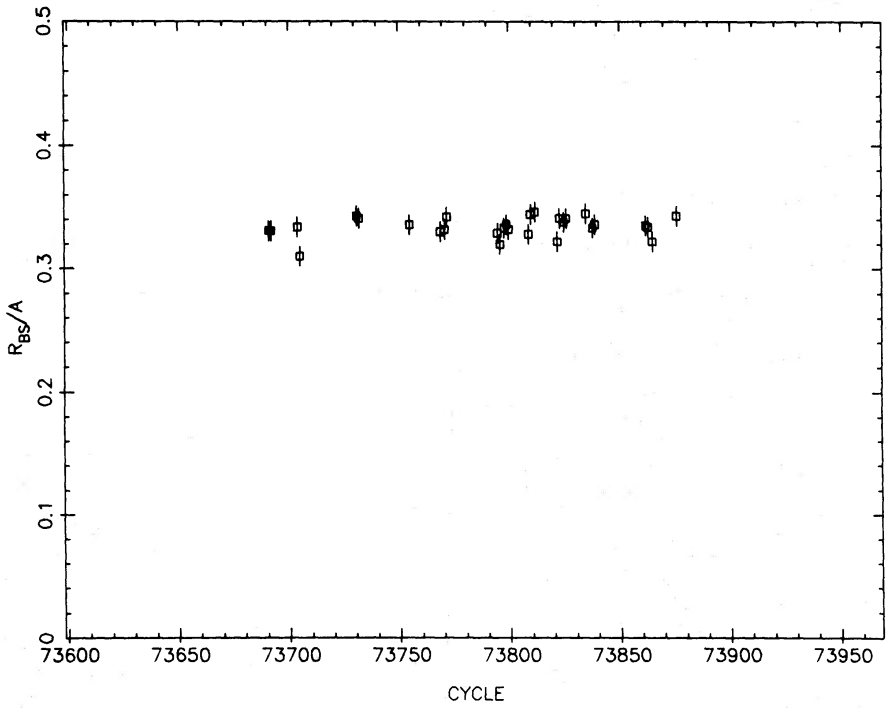

Figure 9. Disc radius R_{BS} (distance of the bright spot from the white dwarf).

with ϕ_{b1} and ϕ_{b4} retaining their original values. This range is not unique; if ϕ_{b1} and ϕ_{b4} are varied, a slightly different range will be found.

The mean light curves of the disc, the bright spot and the white dwarf are shown in Fig. 8 for $f_{disc}=0.72$, $\phi_{b2}=0.0165$, $\phi_{b3}=0.0752$. These light curves are not unique, but the small parameter range and the limited effect they have on the shape of the light curve means that the major features of the component light curves will always be the same. Minimum light in the disc light curve is now at phase 0.004 ± 0.005. That minimum light in Fig. 2 is seen to occur later than this at phase ~0.014, arises because the ingress of the bright spot continues past phase 0.0. The uneven shape of disc egress reflects a true variability in the shape of the standstill between ϕ_{w4} and ϕ_{b3}, and can be seen in the individual cycles [Fig. 1(a)]. The light curve is not, however, symmetric indicating that the surface brightness distribution of the disc is asymmetric.

The reconstruction of the bright spot light curve, given in Fig. 8, clearly shows an extended tail at the end of ingress. Our range of ϕ_{b2} indicates that the tail is azimuthally extended in the direction of rotation. This reflects the radiative cooling of material swept away from the point of collision between the stream and the edge of the disc. This does not change our conclusion that the centre of the stream passes through the light centre (and not upstream from *LC*) since Fig. 5(b) shows clearly that increasing ϕ_{b2} does not change any of the constraints upstream from *LC*. Some light can always be seen in the bright spot light curve, showing that there is an isotropic component in addition to the anisotropic component caused by foreshortening.

5.2 ECLIPSE MAPPING OF THE QUIESCENT DISC

Fig. 9 makes clear that the disc radius, as measured by the radius vector of the bright spot, does not vary significantly during our observations. In addition the flux from the disc varies only slowly (see Section 6). Therefore it seems that the structure of the disc did not change greatly during our observing run and so the mean disc light curve is a valid representation of the disc.

We used the eclipse mapping method, developed by Horne (1985), to reconstruct the white light surface brightness distribution in the accretion disc from the disc light curve (shown in Fig.

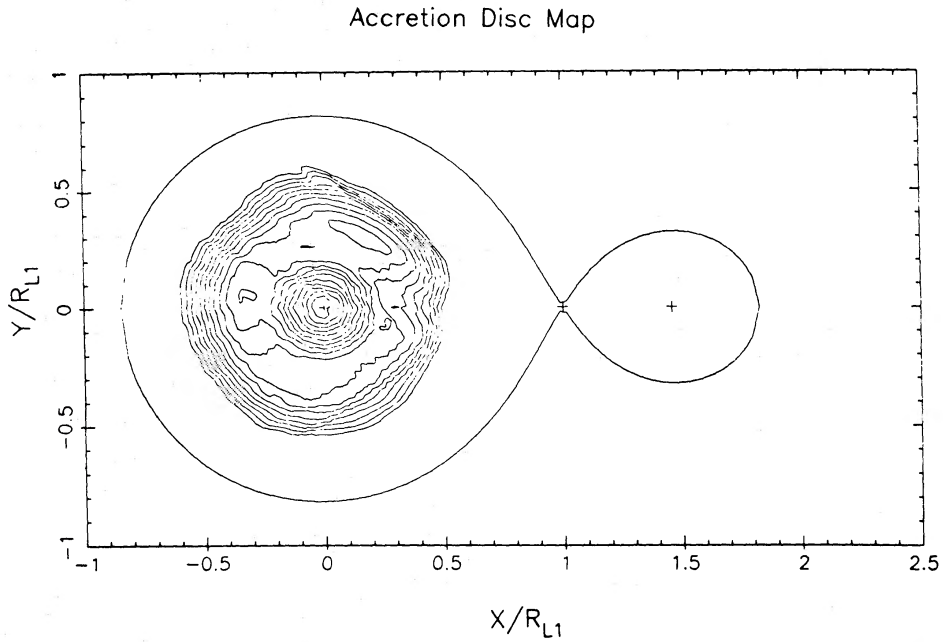

Figure 10. Contour map of the accretion disc. The scale is logarithmic and the interval between contours is 0.08 decades.

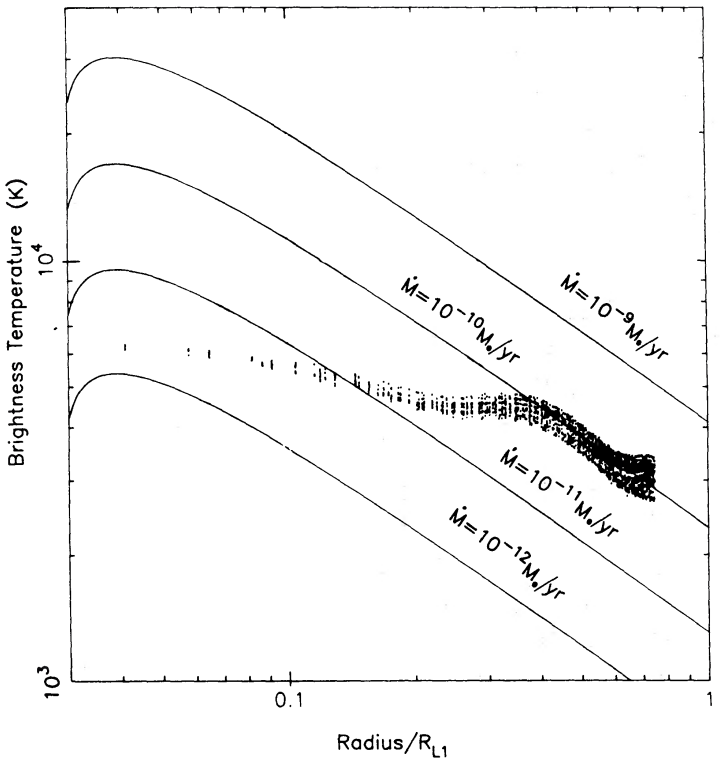

Figure 11. Brightness temperature in the disc. Models of steady state optically thick discs for several mass transfer rates are also shown.

8). The reconstructed image of the disc is shown in Fig. 10 which shows that the intensity increases smoothly to a maximum at the centre of the disc.

We express the surface brightness at each point in the image as a blackbody brightness temperature, T_{BR}, in the same way as for the bright spot in Section 4.1. We neglected interstellar reddening since *IUE* spectra of Z Cha in outburst have shown that $E(B-V)<0.05$ mag (Verbunt, private communication). The brightness temperature distribution is shown in Fig. 11 where it is compared with steady state models for optically thick blackbody discs where

$$T_e^4=3GM_{WD}\dot{M}R^{-3}\{1-\sqrt{(R_{WD}/R)}\}/8\pi\sigma$$

(e.g. Pringle 1981). T_{BR} was also calculated using stellar atmospheres (Gunn & Stryker 1983), and an increase in the brightness temperatures of <1000 K was seen with the shape of the distribution remaining the same. The actual effective temperature, T_e, will lie somewhere between the two cases. The observed surface brightness distribution clearly falls off much more slowly with radius than expected for the $T\sim R^{-3/4}$ law.

The light arising from each point on the disc surface may include emission from both optically thick and optically thin gas. The effective temperature of the optically thick gas must be less than the observed brightness temperature, for otherwise its contribution alone would exceed the observed surface brightness. The brightness temperature correspondingly places an upper limit on the local mass transfer rate in the optically thick component of the disc. The upper limits range from $10^{-11.7}M_\odot$/yr near the centre of the disc to $10^{-9.9}M_\odot$/yr near the outer rim, as may be seen from Fig. 11. For comparison the accretion rate during outburst was an order of magnitude higher at $10^{-8.9}M_\odot$/yr (Horne & Cook 1985).

Were we to assume that the disc is optically thick, the wide range in $\dot{M}$ required by the brightness temperature profile would imply that material is building up in the outer disc during

quiescence. However, the maximum mass transfer rate into the bright spot, $\dot{M}_{BS}=10^{-10.23}\,M_{\odot}/\mathrm{yr}$, is too small to support this interpretation. Further, the colour temperature at minimum light, when only the outer disc is visible (~8500 K) greatly exceeds the brightness temperature in the outer disc, and therefore if the disc were optically thick, it would provide more light than is observed.

We prefer the alternative interpretation, that the quiescent disc is optically thin. In this case, the disc brightness temperatures are given by

$$\langle B_\nu(T_{BR})\rangle=\langle B_\nu(T_{Kin})\{1-\exp(-\tau_\nu/\cos i)\}\rangle,$$

where τ_ν is the optical depth measured vertically through the disc, T_{Kin} is the kinetic temperature of the gas, and $\langle\,\rangle$ denotes the appropriately weighted average over the bandpass (see Section 4.1). Since $B_\nu(T_{BR})<B_\nu(T_{Kin})$, T_{Kin} must be greater than T_{BR} and indeed models of optically thin discs have $T_{Kin}\sim 8000$ K (Williams 1980; Tylenda 1981) which is greater than our brightness temperatures. In the optically thin case the disc may be close to a steady state.

Although we cannot determine T_{Kin} and τ_ν separately from the brightness temperature in our single bandpass, we note that with multicolour surface brightness distributions of the disc $T_{Kin}(R)$ can be found and when combined with $T_{BR}(R)$, the optical depth $\tau(R)$ can be calculated. The kinetic temperatures and the hydrogen number density needed to produce this optical depth give the surface density $\Sigma(R)$. The effective temperature T_e, given by

$$\sigma T_e^4=\pi\int B_\nu(T_{Kin})\{1-\exp(-\tau_\nu)\}\,d\nu$$

allows the dissipated energy and hence the viscosity constant $\alpha(R)$ to be calculated.

6 Secular variations of the components

We have previously found that the position of the bright spot remains approximately constant [Figs 6(b) and 9] and that there are no significant variations in the sizes of the bright spot and white dwarf (Figs 5 and 7) throughout our observations. It is also of interest to examine the variability in the fluxes of the white dwarf, the bright spot and the disc.

The flux densities of the white dwarf and compact bright spot in ingress and egress have been found in each cycle by the same technique as described in Sections 3.1 and 5.1. Figs 12(a) and (b) show these fluxes; the uncertainties in each are those propagated from the uncertainties (rms) in the contact phases. There is no significant secular variations in the fluxes of either component.

In 13 of the 17 white light curves obtained at CTIO, the white dwarf is fainter at the time of its ingress (0.63 ± 0.02 mJy) than it is at egress (0.70 ± 0.02 mJy). Statistical uncertainties of 0.02 mJy are too small to account for this apparent change in brightness. Systematic errors in the white dwarf flux density, such as might be caused by the proximity of the bright spot and white dwarf ingresses, are believed to be small because the two ingresses are well separated in the mean light curve. The white dwarf light may be partially obscured at the time of its ingress by optically thin gas thrown up above the disc plane from the region around the bright spot.

As expected the mean flux of the compact part of the bright spot in ingress, 0.38 mJy, is greater than that in egress, 0.30 mJy (due to the orbital hump). There are also wide differences between individual measurements of both the compact bright spot and the white dwarf. Some of these differences may arise from uncertainties in the contact phases or, if there is a boundary layer around the white dwarf its brightness could well change rapidly ($\leqslant$5 min) and cause the observed changes in white dwarf flux (though one would expect the radius to change as well). Flickering from other parts of the system may affect the measurements of the fluxes of both the white dwarf

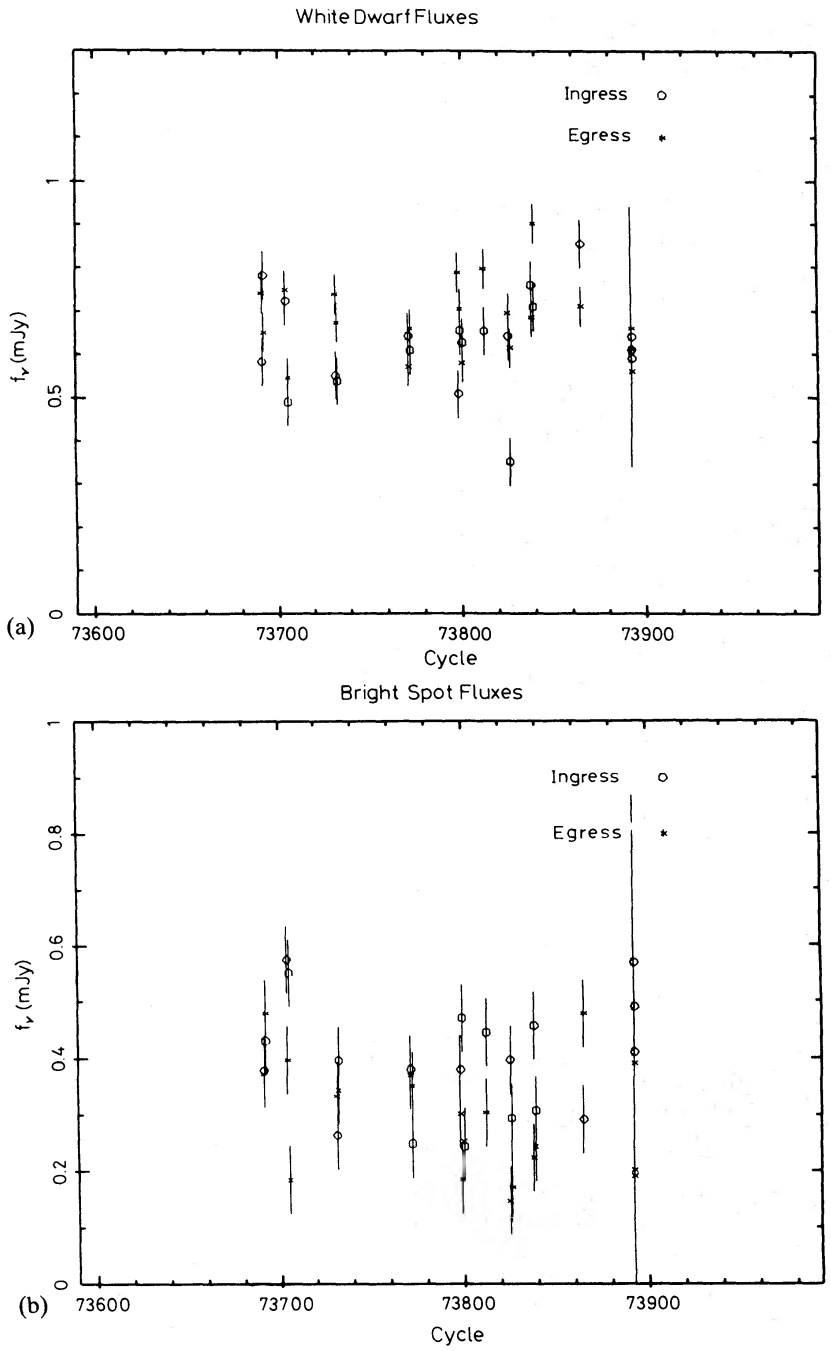

Figure 12. Ingress and egress fluxes. (a) white dwarf, (b) compact part of bright spot. The final measurement is done in U, B and R rather than white light.

and bright spot. The uncertainties shown correspond only to the rms in the contact phases and do not include the effects of flickering during white dwarf or bright spot ingress and egress.

In addition to measuring the fluxes in ingress and egress we have measured the fluxes at phases −0.13 (hump maximum), 0.13 (standstill) and 0.014 (minimum light) in each cycle. The measured fluxes are plotted in Fig. 13. Differences of up to ~0.4 mJy are seen in the flux of each component from cycle–cycle. Scatter in the sky measurements could account for up to 0.15 mJy variations. The flux density measurements for the mean U, B, W and R light curves are given in Table 10.

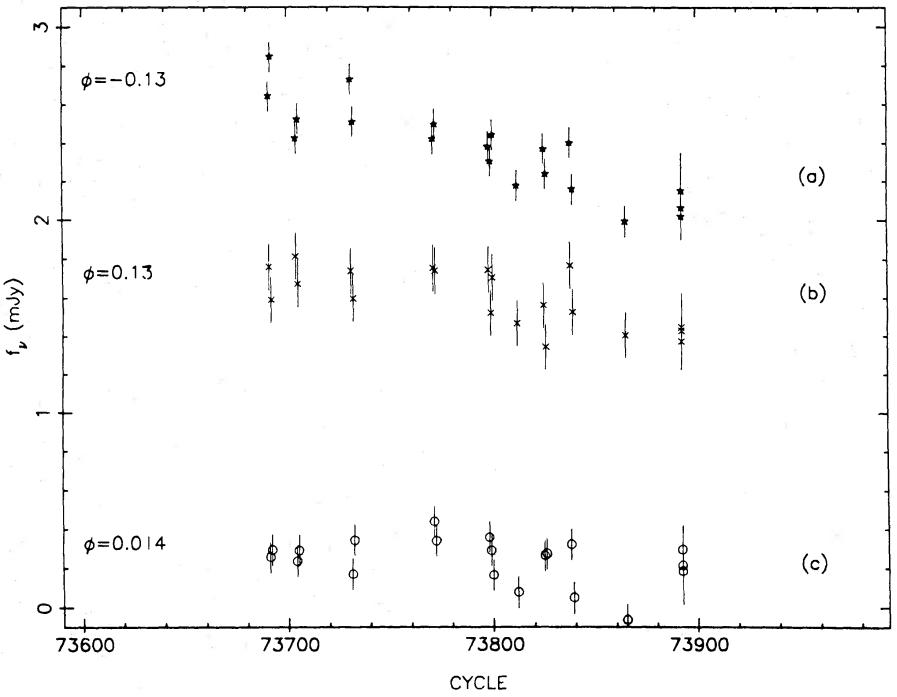

Figure 13. Fluxes at different phases. (a) Orbital hump maximum $\phi=-0.13$. (b) After the end of the orbital hump $\phi=0.13$. (c) Minimum light $\phi=0.014$. The final measurement is done in *U*, *B* and *R* rather than white light.

Table 10. Flux densities of mean light curves.

FILTER	WHITE DWARF		BRIGHT SPOT		HUMP MAXIMUM	MINIMUM	STANDSTILL
	INGRESS	EGRESS	INGRESS	EGRESS	(φ=−0.13)	(φ=0.014)	(φ=0.13)
	(mjy)	(mjy)	(mjy)	(mjy)	(mjy)	(mjy)	(mjy)
U	0.61	0.66	0.49	0.19	2.02	0.18	1.37
B	0.64	0.61	0.57	0.20	2.15	0.21	1.43
W	0.63	0.70	0.38	0.30	2.41	0.24	1.63
R	0.59	0.56	0.41	0.39	2.06	0.30	1.43

There is only marginal evidence for a systematic change in the flux at minimum light or at standstill, but there is a 99.9 per cent probability that the flux at hump maximum is decreasing. This flux is a superposition of the light from the disc, white dwarf and bright spot, which individually do not decrease significantly. It seems plausible therefore that the change in the flux at hump maximum is due to the superposition of slow changes in the disc, white dwarf and bright spot fluxes. The least squares straight line fits to these data show that, within 2σ limits this situation is not ruled out as long as both the bright spot and disc fluxes decrease.

7 Conclusions

This investigation of 29 white and 2 *UBR* light curves of Z Cha in quiescence has shown that:

(i) Theoretical stream trajectories (Lubow & Shu 1975) pass through the observed light centre of the bright spot for $0.146<q<0.153$, with corresponding inclinations of $81°.9>i>81°.6$.

(ii) The position (radius and azimuth) and structure of the bright spot are approximately constant through our observations. The bright spot is however smaller than those previously found. There is an extended tail formed by material swept downstream by rotating material in the

disc. The anisotropic component follows a cosine law suggesting that the bright spot is 'painted' on to the edge of the disc. There is an isotropic component in the bright spot light curve in addition to the cosine shaped hump.

(iii) The white dwarf radius is $0.0195\pm0.0004A$, and its mass $0.54\pm0.01\,M_\odot$. Hence the secondary mass is $0.081\pm0.003\,M_\odot$. The corresponding system parameters are listed in Table 9. If the radiation comes from an approximately spherical boundary layer rather than the white dwarf proper, these mass estimates are lower limits.

(iv) The flux density at the peak of the orbital hump declines in brightness from ~2.8 to 2.0 mJy over a period of 16 day.

(v) We present a map of the brightness distribution in the quiescent disc. This shows that the disc intensity increases smoothly to a maximum at the centre of the disc. However the slope of the radial profile is much flatter than that expected for a steady state, optically thick disc. The brightness temperature distribution gives upper limits at each radius on the temperature and mass transfer rate (see Fig. 11) of any optically thick component in the quiescent disc. The colours of the disc show there must be an optically thin component.

(vi) The mass transfer rate into the bright spot is somewhere between $10^{-10.23}\,M_\odot$/yr and $10^{-10.63}\,M_\odot$/yr. The mass transfer rates through the disc, $\dot{M}\leqslant10^{-9.9}\,M_\odot$/yr, are much less than that found in outburst where $\dot{M}=1\times10^{-8.9\pm0.3}\,M_\odot$/yr (Horne & Cook 1985).

Acknowledgments

The observations were carried out while RAW was Lindheimer Fellow in Astronomy and Astrophysics at Northwestern University and GB a SERC Postdoctoral Research Fellow at the Institute of Astronomy in Cambridge. We thank Frank Verbunt for determining the reddening to Z Cha and Jim Pringle, Tom Marsh, Frank Verbunt and Allyn Tennant for useful discussions. We also thank Mike Cook for suggesting the observations. We gratefully acknowledge CTIO for the allocation of telescope time and thank the director and support staff. We thank Chris Godfrey and Richard Sword for help with the figures. Reductions and analysis of the photometry were carried out on the Cambridge node of the SERC STARLINK network.

References

Bailey, J., 1979. *Mon. Not. R. astr. Soc.,* **187,** 645.
Bailey, J., Sherrington, M. R., Giles, A. B. & Jameson, R. F., 1981. *Mon. Not. R. astr. Soc.,* **196,** 121.
Batten, A. H., 1973. *Binary and Multiple Systems of Stars,* Pergamon Press, Oxford.
Cook, M. C., 1983. *PhD thesis,* University of Cambridge.
Cook, M. C., 1985. *Mon. Not. R. astr. Soc.,* **216,** 219.
Cook, M. C. & Warner, B., 1982. *Mon. Not. R. astr. Soc.,* **196,** 55P.
Cook, M. C. & Warner, B., 1984. *Mon. Not. R. astr. Soc.,* **207,** 705.
Fabian, A. C., Lin, D. N. C., Papaloizou, J., Pringle, J. E. & Whelan, J. A. J., 1978. *Mon. Not. R. astr. Soc.,* **184,** 835.
Fabian, A. C. Pringle, J. E., Whelan, J. A. J. & Bailey, J. A., 1979. *Variable Star Research, IAU Collm. 46,* eds Bateson, F. M., Smak, J. & Urch, I. H., University of Waikato, Hamilton, New Zealand.
Flannery, B. P., 1975. *Mon. Not. R. astr. Soc.,* **170,** 325.
Gunn, J. E. & Stryker, L. L., 1983. *Astrophys. J. Suppl.,* **52,** 121.
Hamada, T. & Salpeter, E. E., 1961. *Astrophys. J.,* **134,** 683.
Horne, K. D., 1985. *Mon. Not. R. astr. Soc.,* **213,** 129.
Horne, K. D. & Cook, M. C., 1985. *Mon. Not. R. astr. Soc.,* **214,** 307.
Lubow, S. H. & Shu, F. H., 1975. *Astrophys. J.,* **198,** 383.
Lynden-Bell, D. & Pringle, J. E., 1974. *Mon. Not. R. astr. Soc.,* **168,** 603.
Mumford, G. S., 1971. *Astrophys. J.,* **165,** 369.
Paczynski, B., 1977. *Astrophys. J.,* **216,** 822.

Patterson, J., 1981. *Astrophys. J. Suppl.*, **45,** 517.
Pringle, J. E., 1975. *Mon. Not. R. astr. Soc.*, **170,** 633.
Pringle, J. E., 1977. *Mon. Not. R. astr. Soc.*, **178,** 195.
Pringle, J. E., 1981. *Ann. Rev. Astr. Astrophys.*, **19,** 137.
Rayne, M. W. & Whelan, J. A. J., 1981. *Mon. Not. R. astr. Soc.*, **196,** 73.
Ritter, H., 1980. *Astr. Astrophys.*, **86,** 204.
Smak, J., 1979. *Acta Astron.*, **29,** 309.
Stone, R. P. S. & Baldwin, J. A., 1983. *Mon. Not. R. astr. Soc.*, **204,** 347.
Tylenda, R., 1981. *Acta Astron.*, **31,** 127.
Vogt, N., 1981. *Astrophys. J.*, **252,** 653.
Warner, B., 1974. *Mon. Not. R. astr. Soc.*, **168,** 235.
Williams, R. E., 1980. *Astrophys. J.*, **235,** 939.
Wood, J. H., Irwin, M. J. & Pringle, J. E., 1985. *Mon. Not. R. astr. Soc.*, **214,** 475.